JOURNAL OF MATERIALS SCIENCE **39** (2004) 4495–4505

On the mechanical behavior of carbon-carbon optic grids determined using a bi-axial optical extensometer

D. ZHANG
Department of Mechanics, Shanghai University, 99 Shangda Road, Shanghai, 200436, People's Republic of China

D. AROLA*, P. G. CHARALAMBIDES
Department of Mechanical Engineering, University of Maryland Baltimore County, 1000 Hilltop Circle, Baltimore, MD 21250
E-mail: darola@engr.umbc.edu

M. C. L. PATTERSON
Advanced Ceramics Research Inc., 3292 E. Hemisphere Loop, Tucson, AZ 85706-5013

Ion engines accelerate electrically charged plasma through two optic grids and emit the ions as exhaust. The process facilitates propulsion without use of chemical propellants. Braided carbon fiber reinforced composite ($C_{(f)}/C$) optics are presently being considered for use as the accelerator and screen grids in ion propulsion engines. In this study the mechanical behavior of four candidate tow configurations proposed for the grids of NASA's Evolutionary Xenon Thruster (NEXT) were examined. A new bi-axial optical extensometer based on Digital Image Correlation (DIC) was developed and employed in determining the in-plane strain distribution resulting from uniaxial tension. The effective elastic modulus ranged from 4 GPa to 10 GPa at the onset of deformation. The stiffness either increased or decreased with further elongation as a result of bending of the axial tows and corresponding unit cell distortion. The transverse strain and Poisson's ratio of the panels were found to be a function of the tow dimensions and bonding between longitudinal and transverse tows.

1. Introduction

Research efforts aimed at extending interstellar space travel have recently been focused on the development and performance of ion propulsion engines. One approach being pursued is an array of ion propulsion engines. This design is similar to the successful thruster developed by NASA's Solar Electric Propulsion Technology Applications Readiness (NSTAR) program that was flown on Deep Space One [1, 2]. Unlike traditional chemical rocket engines, ion engines exhaust charged inert gasses to generate thrust forces. The current technology incorporates Molybdenum accelerator and screen grids through which ions from charged plasma are accelerated. According to their intended application and conditions of operation, the life of these engines and ability for delivering sustained performance are primary concerns.

As part of the NSTAR program the ion propulsion grids have been subjected to an extended performance evaluation and life assessment [3, 4]. Results from an examination of the Molybdenum grids demonstrated that sputter erosion was an outstanding problem that limited the operating life of ion optic engines [5]. NASA's Evolutionary Xenon Thruster (NEXT) system will require the engine to sustain high power (10 kW) over roughly 100,000 h of service. These operating conditions are far outside the scope of what presently appears possible with even state-of-the-art Molybdenum grids. In addition to erosion resistance, the accelerator and screen grids are separated by less than 1mm and need to survive severe vibration and impact loads that are experienced during launch.

Due to their exceptional resistance to sputter erosion and high strength and stiffness to weight ratios carbon fiber reinforced composites ($C_{(f)}/C$) have been considered as a viable material for the accelerator and screen optic grids. Uniaxial carbon fiber dished, lay-ups have previously been mechanically drilled [6], but the drilling of so many holes severed the fibers causing distortion and severe weakening of the grids. Subsequent vibration tests demonstrated a critical lack of structural integrity in the hardware [7]. Continuous woven carbon fiber composites may serve as an ideal material provided that an adequate grid geometry and screen

*Author to whom all correspondence should be addressed.

configuration is obtained. The complex weave geometry of the grids has complicated the design and manufacture of these components. Furthermore, traditional methods of evaluating the constitutive behavior are not readily applicable due to the open cell network and irregular surface geometry resulting from weaving. Thus, there are outstanding manufacturing issues associated with development of the required grid configurations and consequent performance concerns that remain to be addressed.

In this study the mechanical behavior of prototype $C_{(f)}/C$ optical grids was investigated. The primary objective was to characterize the elastic properties and to develop an understanding of differences in mechanical behavior between four candidate tow configurations recently proposed for the NEXT system grids. A biaxial optical extensometer was developed to evaluate the in-plane response of the specialized weaves under uniaxial tension. The optical extensometer is based on principles of Digital Image Correlation (DIC). Results from the experimental analysis were used to determine the effective elastic constants and to examine constitutive responses in terms of the unit cell behavior. Mechanical properties of the optic grids are presented and advantages of the optical approach for evaluating the mechanical behavior are highlighted.

2. Background

Extensometers are one of the most common instruments used in characterizing the constitutive behavior of engineering materials. The conventional electrical-mechanical types are physically attached to the material and are required to maintain contact throughout deformation. However, compliant materials (e.g. soft tissues) and materials with irregular surface geometry (e.g. woven composites) can complicate the use of instruments requiring contact with the substrate. Optical extensometers provide a non-contact method for displacement or strain measurement and are often based on interferometry (laser-based) or video tracking. Laser-based extensometers [8–12] generally require complicated surface preparation and are often limited by the coherent length of the laser. Development of the video extensometer [13–16] has expanded the application of optical extensometers in engineering practice. Generally, two parallel reference lines are placed onto the specimen's surface, which are monitored while the specimen undergoes deformation. Although the surface preparation and associated system is simple, video extensometers can only quantify the average strain between the reference lines. As a result, the strain distribution is assumed to be uniform within the effective gage length, which is established by placement of the reference markers.

The optical extensometer utilized in this investigation is based on Digital Image Correlation (DIC) and overcomes limitations of contact and video-based extensometers [17, 18]. Digital image correlation is a unique optical technique that uses image recognition to quantitiatively analyze and compare digital images acquired from the surface of a substrate. Depending on the natural contrast variation of the substrate, a simple surface preparation may be used to enhance the grayscale distribution and establish a "speckled" surface with high contrast. Digital images acquired before and after deformation document the "speckle" distribution and can be represented by the grayscale distribution. The light intensity distribution at each point on the surface is unique and the distribution in light intensity about a particular point (x, y) can be described by the grayscale matrix $F(x, y)$ over a selected subset of the digital image. With deformation of the object each position of the surface (x, y) is assumed to exist at a new location (x^*, y^*). The in-plane surface displacement can be determined by finding the position of the light intensity distribution $F^*(x^*, y^*)$ that most closely resembles the original distribution $F(x, y)$. A search is performed to find the location on the "deformed" image (after deformation) with grayscale distribution that is most consistent with that on the original "undeformed" (before deformation) image. The location of $F^*(x^*, y^*)$ can be obtained by finding the position with maximum correlation coefficient (C) according to

$$C = \frac{\langle F \cdot F^* \rangle - \langle F \rangle \cdot \langle F^* \rangle}{[\langle (F - \langle F \rangle)^2 \rangle \cdot \langle (F^* - \langle F^* \rangle)^2 \rangle]^{\frac{1}{2}}} \qquad (1)$$

where F, and F^* are the grayscale matrices of the subset at position (x, y) in the undeformed image and (x^*, y^*) in the deformed image, respectively. The symbol $\langle\rangle$ in Equation 1 implies the mean value of the elements in the matrix. The search for the point with maximum correlation coefficient ($C_{\max}$) on the deformed image is initially implemented at integer pixel locations. When the location with maximum correlation coefficient is found the search may be continued in the sub-pixel domain for increased precision. It is important to recognize that the correlation is established at each pixel over the field of view and is conducted using a subset of the image (correlation window) according to Equation 1. For instance, in a field of view of 25.4 mm by 20 mm documented with spatial resolution of 640 by 480 pixels, a correlation window of 21 × 21 pixels is often used. To increase precision futher, the search for location with maximum correlation can be continued from the integer pixel in successive search steps from 0.1 pixels, 0.01 pixels to a final step of 0.001 pixels. In that manner a precision of 0.001 pixels can be achieved. There are different search strategies available for finding the location with maximum correlation coefficient, the most common of which is the Newton-Raphson method [19]. In this study a "fast-search strategy" was used in identifying the position with maximum correlation [20].

If the out-of-plane displacement is small and can be neglected, the relationship between (x, y) and (x^*, y^*) can be written as

$$\begin{aligned} x^* &= x + u + \frac{\partial u}{\partial x}\Delta x + \frac{\partial u}{\partial y}\Delta y \\ y^* &= y + v + \frac{\partial v}{\partial x}\Delta x + \frac{\partial v}{\partial y}\Delta y \end{aligned} \qquad (2)$$

where u, v are displacements with respect to the x and y axes; $\partial u/\partial x$, $\partial v/\partial y$ are the strains in x and y directions and the combination of $\partial u/\partial y$ and $\partial v/\partial x$ represent the shear strain at the location of (x, y), respectively. Generally, the out-of-plane displacement should be limited to the deformation resulting from Poisson's effects. Note that the displacement components in Equation 2 are much greater than the corresponding partial derivatives. Thus, strain in the x and y directions can be deduced from the displacement difference between two locations with relative distance of dx and dy as

$$\varepsilon_x = \frac{du}{dx}$$
$$\varepsilon_y = \frac{dv}{dy} \quad (3)$$

Digital image correlation is generally used as a full-field technique to quantify the displacement/strain distribution over the entire field of view. In application to materials with an array of reinforcing ligaments and open cells there are portions of the image where a correlation would be meaningless since these areas are not comprised of the substrate. In these instances DIC cannot be applied in the conventional manner. The correlation process can be performed using a selected set of points that correspond to specific locations within the field of view. In this study a unique approach was adopted for selecting locations in the optical image of the composite grids under investigation to quantify the in-plane displacements and strains in two orthogonal directions.

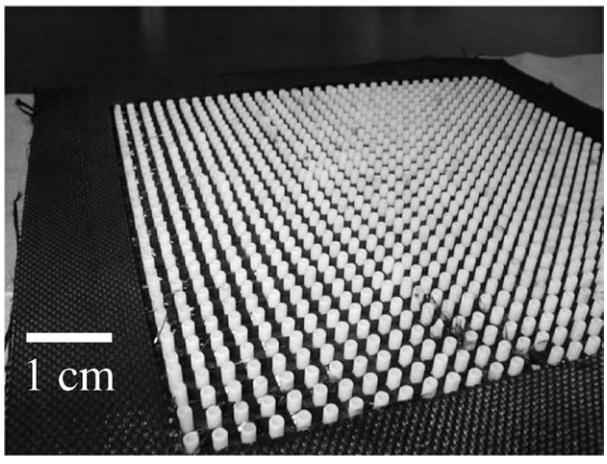

(a)

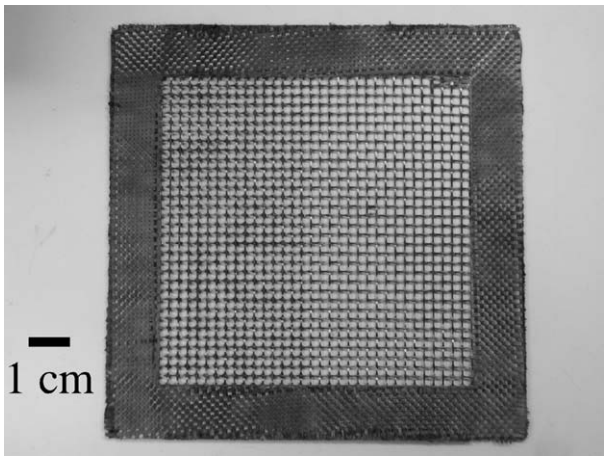

(b)

Figure 1 The braided composite screen grid: (a) accelerator grid on the graphite mandrel woven about the alumina pins (oblique view) and (b) the grid with carbon fiber mat border.

3. Materials and methods

One pair of braided $C_{(f)}/C$ optic grid test plates was manufactured to enable an evaluation of the mechanical properties. Each grid was approximately 15 cm square and produced with two tow configurations that served as candidate designs for the accelerator and screen grids. Both of the grids were plain weaves incorporating T-300 carbon fibers oriented in a square array for ease of weaving. The grid was woven onto a graphite mandrel around alumina pins (Fig. 1a). The two orthogonal directions defined by the weave geometry are referred to here as the axial and transverse directions. The hole-to-hole spacing was 4.60 mm with a 4.04 mm diameter and 2.39 mm diameter pin size for the screen and accelerator grids, respectively. A carbon mat of approximately 25 mm width was placed around the edge of the grid on both the upper and lower surfaces to stiffen the edges of the woven grid during the Chemical Vapor Infiltration (CVI) process (Fig. 1b). The woven fiber preforms were placed horizontally into a vacuum chamber, evacuated to approximately 5 torr and pyrolytic carbon deposited for a period of approximately 60 h under dilute infiltration conditions.

In the screen grid two fiber variations were investigated, one with 9 k fibers in both the axial and transverse orientations and the other having 18 k fibers and 9 k fibers in the axial and transverse directions, respectively. Similarly, two fiber variations of the accelerator grid were investigated, one with 24 k fibers in both directions and the other with 48 k fibers and 24 k fibers in the axial and transverse directions, respectively. In all four configurations under consideration the axial direction was defined parallel to the tows with maximum fiber count. The screen and accelerator grids with equal axial and transverse fiber counts were considered "balanced", while the grids with unequal fiber count (i.e. larger axial fiber count) were regarded as "hybrid" systems. Both grids were developed with the cells placed in a square arrangement, which is consistent with the NEXT requirements. The grid thickness was greater than that envisioned for the NEXT design. Cell dimensions of the grids are shown in Fig. 2a. The grids exhibited a distinctly woven topography after CVI but showed good fiber tow infiltration and a thin matrix coating of approximately 10 to 20 microns.

Straight-sided tensile specimens were prepared from the accelerator and screen grids. The longitudinal axis was defined on each specimen by the panel's axial tows (direction of tows with maximum fiber count). As a result of the different tow dimensions utilized, four different specimen types were prepared including a "balanced" and "hybrid" configuration of the accelerator and screen grids. The tensile specimens consisted of four or five cells in the transverse direction resulting

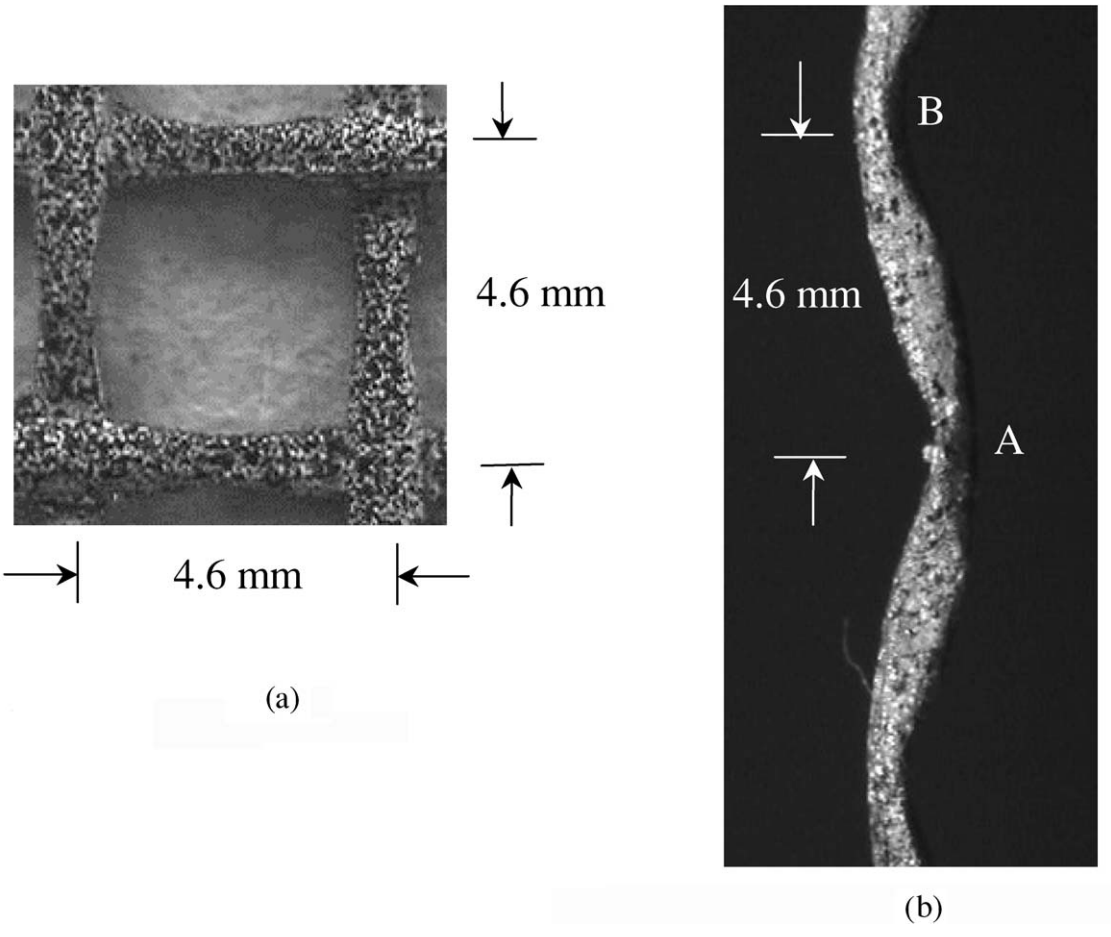

Figure 2 Cell dimensions and tow curvature of the grids. The system used for illustration in this figure is the screen grid: (a) tow spacing and (b) the sinusoidal shape of a single tow (side view).

in specimens with 20 mm width and approximately 150 mm length including the gage and grip sections. All sectioning was conducted using diamond impregnated abrasive slicing wheels with #220 mesh under continuous water-based flood coolant. A total of 8 tensile specimens were sectioned from the 2 grids. In addition, single axial tows were cut from the balanced screen (9 k fibers) and balanced accelerator grid (24 k fibers) to examine mechanical behavior of the axial tows independent of potential effects from the transverse fibers. Since the panels were braided with plain weave, the tow maintained a distinct sinusoidal shape as evident from the size view of a single screen tow in Fig. 2b.

Aluminum end tabs were bonded to both ends of the tensile specimens to facilitate the use of compression grips for administering the axial loads. Grip surfaces were prepared as described by Carlsson and Pipes [21] and bonded using a high strength epoxy adhesive.[1] In addition, the surface of each specimen was prepared to enable application of DIC. One surface of the specimens was sprayed with matte white enamel paint, followed by another very light coat of black enamel paint. The procedure resulted in a matte white surface laden with a random distribution of black dots.

Tension tests were performed using a universal testing system[2] with full-scale load range of 1200 N. The load was administered under displacement control at a strain rate of 5×10^{-5} s^{-1} until reaching a maximum of 1000 N or failure of the specimen. A piece of paper was attached to the back surface of the specimens (opposite to that facing the camera) to eliminate problems associated with defocusing of the camera through open holes of the grids. The universal test system offered output of a 5 volt DC signal at the onset of the tension from its digital I/O port. A connection was made from this I/O port to the standard parallel I/O port of a second computer that was used to capture digital images. The axial load and DC output was used as a trigger signal to initiate the data acquisition process. Synchronization of digital images from the optical extensometer with the axial load was achieved in this manner and insured accuracy of the stress/strain response. The maximum framing rate available from the image acquisition system as configured was 9 Hz.

The optical equipment and accompanying items used for acquisition of digital images include a Panasonic CCD camera with 10X Computar zoom lens, a PCVISION "plus" frame grabber and a DELL computer. An incoherent light source was also used to uniformly illuminate the object's surface. The CCD camera was placed normal to the illuminated surface approximately 400 mm from the specimen. A picture of the experimental arrangement is shown in Fig. 3. The load and sequential digital images were both documented with a sampling frequency of 0.5 Hz. The load history and sequential digital images were stored on separate

[1]Devcon, ITW Performance Polymers.

[2]Instron Dynamite, Model 8841.

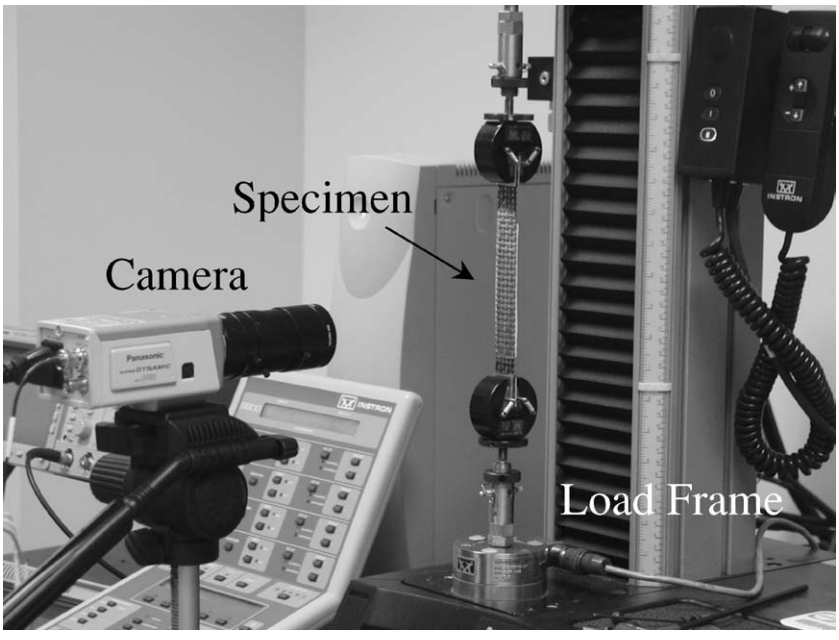

Figure 3 Experimental arrangement for the tensile tests.

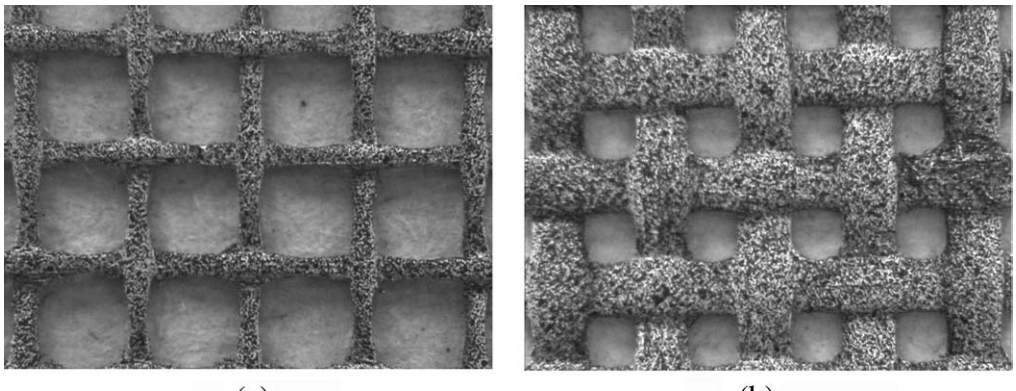

Figure 4 Field of view for the tensile specimens. The window measures 25.4 mm by 20 mm and is digitized with spatial resolution of 640 by 480 pixels. Note that the field of view is comprised of 9 unique cells: (a) screen and (b) accelerator.

computers, which were synchronized by the digital I/O of the universal test system. The actual field of view acquired using the camera was 20 mm by 15 mm and was digitized into a sample of 640 by 480 pixels with 256 gray levels. The camera placement and magnification was chosen to ensure that the width of each single tow was greater than 20 pixels (even for the balanced screen grid). An example of the field of view for the screen and accelerator grids is shown in Fig. 4; note that the image is comprised of 12 individual cells.

The displacement distribution in each grid was determined from the digital images acquired during the tensile tests using DIC. The first image taken prior to the application of an axial load represented the "undeformed object". On the first image, a set of points was selected on each of the axial and transverse tows. The distance between adjacent point pairs established the gage length used in estimating the corresponding strain. Two concerns guided the choice of points. The first concern was associated with the correlation window. It was necessary to select points such that the subset of pixels surrounding the point (defining the correlation window) all existed on the tow. For the hybrid and balanced screen panel the selected correlation window was 19 × 19 pixels, whereas the subset size for the accelerator grid was 21 × 21 pixels. The second concern in choosing points was the contribution of axial and bending deformation to the displacement and corresponding strain distribution. The perceived elongation is a function of the axial strain induced by tension and bending strains caused by the sinusoidal tow shape. The contribution from bending is dependent on whether the selected points are on the tensile or compressive portion of the tow. A side view of a single tow is shown in Fig. 2b to illustrate this phenomenon. For sake of discussion the camera is placed to the right of the tow in this figure and perpendicular to the tow's primary axis. With the application of uniaxial tension, the strain detected by DIC at location "A" would consist of the axial strain due to tension and a compressive component of bending strain induced by straightening of the tow. In contrast, the strain detected at location "B" would be larger than that at "A" due to the superposition of the axial strain due tension and a tensile

component of bending strain induced by straightening of the tow.

Through proper choice of points for the correlation process, either the microstrain distribution along the tows or the effective strain response of the tows was available. The microstrain distribution was available by choosing a series of points along the tow, determining the displacement of the individual points and then estimating the strain according to Equation 3. Similarly, the effective axial response of the tows was available from selection of a single pair of points that underwent strain representative of the macroscopic response. In both cases the search for location with maximum correlation was continued to a final step of 0.001 pixels to obtain a precision of 0.001 pixels.

Prior to estimating the elastic constants a preliminary analysis of the strain distribution along the axial and transverse tows was conducted with each grid to find the minimum tow length that must be monitored to accurately represent the effective response. It was found that the strain of both axial and transverse tows was adequately quantified by the total deformation occurring over a minimum of two cells in length. In addition, due to the bending component of strain as previously described, the selected points should coincide with the intersection of axial and transverse tows. Therefore, the "effective" properties of the $C_{(f)}/C$ grids were defined by the macroscopic strain occurring over a gage length of two cells and the intersections between axial and transverse tows were used as the gage marks. The uniaxial strain for each grid was described by the average strain in the axial tows documented within the field of view.

The elastic modulus (E) and Poisson's ratio (ν) of each grid were calculated utilizing the strain measurements. The elastic modulus was quantified using the tangent method and defined over selected regions of the uniaxial response in terms of the engineering stress and engineering strain. Variation in the elastic modulus and Poisson's Ratio were defined in terms of the standard deviation and were evaluated in terms of variation in the stress-strain and strain-strain pairs over the axial load range of interest. In general, the specimens were not taken beyond the proportional limit stress due to the limitations of the universal test system. Two different approaches were used in defining the cross-section area of the grids, namely the "actual" and the "effective" tow section. Definitions for the cross-section were important in quantifying the axial stress resulting from the tensile loads. The actual cross section area was defined as the tow cross-section area multiplied by the number of tows, while the effective tow section was defined as the panel thickness (summation of axial and transverse tow thickness) multiplied by the width of the tensile panel. A description of the tow geometry and measurements used in defining the panel cross-section are shown in Fig. 5. The Poisson's ratio was determined from the ratio of the average strain in the transverse tows and the average strain in the axial tows. The elastic constants for each grid (E, ν) were calculated for grid stresses greater than 2 Ksi to minimize the potential effects of grip slip and seating.

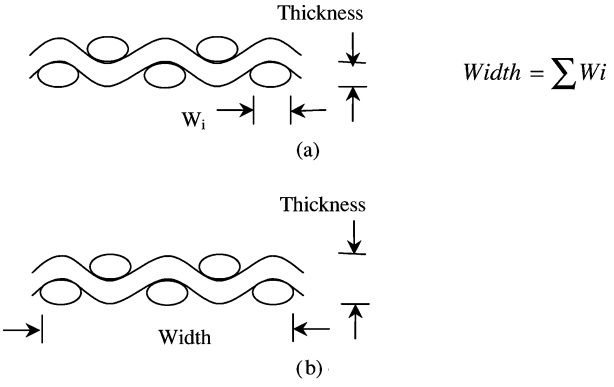

Figure 5 Definition of the grid dimensions used in estimating the cross-section area: (a) actual grid cross-section and (b) effective grid cross-section.

4. Results

The uniaxial stress/strain responses for the specimens prepared from the braided $C_{(f)}/C$ optic grids are presented in Fig. 6. In particular, the responses for the balanced and hybrid screen grids are shown in Fig. 6a and b, respectively. Similarly, the stress/strain responses of the balanced and hybrid accelerator grids are shown in Fig. 6c and d, respectively. The effective tow section was used to estimate the axial stress in this figure. Note that the uniaxial responses for the accelerator grids are demarcated by two different slopes (E_1 and E_2) where $E_1 \leq E_2$. The response of the screen grids exhibited a single effective modulus (E_1) or a bilinear stiffness where $E_2 \leq E_1$. The elastic constants for the grids are listed in Table I. Interestingly, the uniaxial responses of the woven grids were not monotonic but rather oscillated with increasing load. Noise was heard emanating from the specimens while the tensile test was being performed; the noise occurred more frequently with increasing load and was expected to result from debonding of the transverse and axial fibers as well as microcracking damage in the axial tows. Of the four specimen configurations examined the hybrid accelerator grids exhibited the largest primary elastic modulus (E_1). In both the screen and accelerator grids the specimens with hybrid configuration (i.e. larger axial fiber count) exhibited the largest primary elastic modulus. For both the screen grids the elastic modulus decreased with increasing strain while the stiffness of the accelerator grids increased with axial strain. Poisson's ratio was also estimated from the uniaxial response for the four grid configurations and is presented in Table I.

Utilizing the optical extensometer it was possible to examine the strain distribution in each of the axial and

TABLE I Summary of the elastic constants for the screen and accelerator grids

Grid	E_1 (GPa)	E_2 (GPa)	ν_{12}
Screen			
Balanced	8.46 ± 0.70	(N/A)	0.47 ± 0.13
Hybrid	8.59 ± 0.70	2.46 ± 0.77	0.71 ± 0.21
Accelerator			
Balanced	4.07 ± 0.93	9.30 ± 0.47	-0.12 ± 0.08
Hybrid	9.40 ± 1.12	18.41 ± 2.32	-0.32 ± 0.08

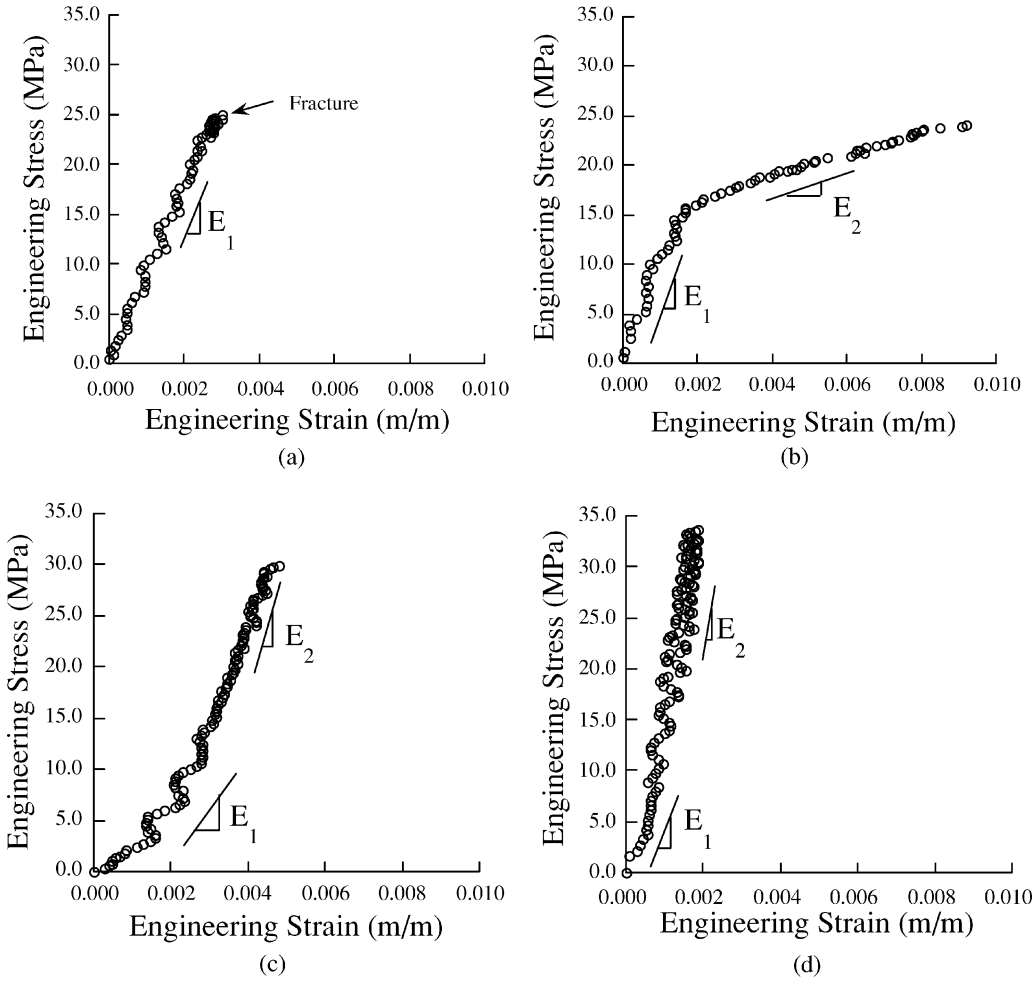

Figure 6 Stress/strain response for the screen and accelerator grids: (a) balanced screen, (b) hybrid screen, (c) balanced accelerator, and (d) hybrid accelerator.

transverse tows with axial loading. For instance, the axial stress-strain response in each of the axial tows for the hybrid screen grid is shown in Fig. 7a; the averaged axial response for this specimen was shown in Fig. 6b. Note that the entire axial response is shown while the averaged axial response in Fig. 6 was truncated at 10% axial strain to facilitate a comparison with the other grid configurations. The corresponding transverse strain response in terms of the axial stress is shown in each of the individual transverse tows of the hybrid screen grid panel in Fig. 7b. Both Fig. 7a and b show that the load distribution in the axial and transverse tows was not uniformly distributed.

Based on differences in constitutive behavior of the accelerator and screen grids and the oscillation in stiffness evident in Fig. 6, the axial stress/strain response in each tow of the accelerator grids was also examined. The stress/strain response for individual tows of the balanced accelerator panel is presented in Fig. 8; the averaged response of the grid was shown in Fig. 6c. Plots for the 5 tows are shown in Fig. 8a–e and correspond to the tows labeled from left to right. Interestingly, the magnitude of oscillation in stiffness is not equivalent in the 5 tows. For example, the magnitude of strain variation in the fourth tow (Fig. 8d) is much less than that of the third tow in Fig. 8c.

The unique constitutive behavior exhibited by the grids and noise emanating from the specimens during axial loading prompted further examination of the mechanical behavior. Therefore, the stress/strain behavior for a single tow from the balanced screen and accelerator grids was examined and is shown in Fig. 9a and b, respectively. The actual tow cross section was used in estimating the axial stress. In comparison to the uniaxial response presented in Fig. 6, the oscillation in stiffness with elongation of the tow was less significant for the separate screen and accelerator tows than for the tensile specimens comprised of a group of parallel tows bound by transverse tows. In addition, the elastic modulus of the single tows estimated for small strains ($\varepsilon \leq 0.002$ m/m) was much less than that for T-300 fibers ($E_{\text{axial}} = 370$ GPa) indicating the significance of bending deformation of the tows on the uniaxial response. Both the individual screen and accelerator tows in Fig. 9 were loaded to failure. Although the tows maintained their sinusoidal shape even after failure, the tows had delaminated along the length due to interlaminar shear as evident in Fig. 10.

5. Discussion

The mechanical behavior of specially designed woven carbon fiber composite optical grids with four different tow configurations was investigated. Straight-sided specimens were obtained from the grids and subjected to uniaxial tension. The constitutive behavior

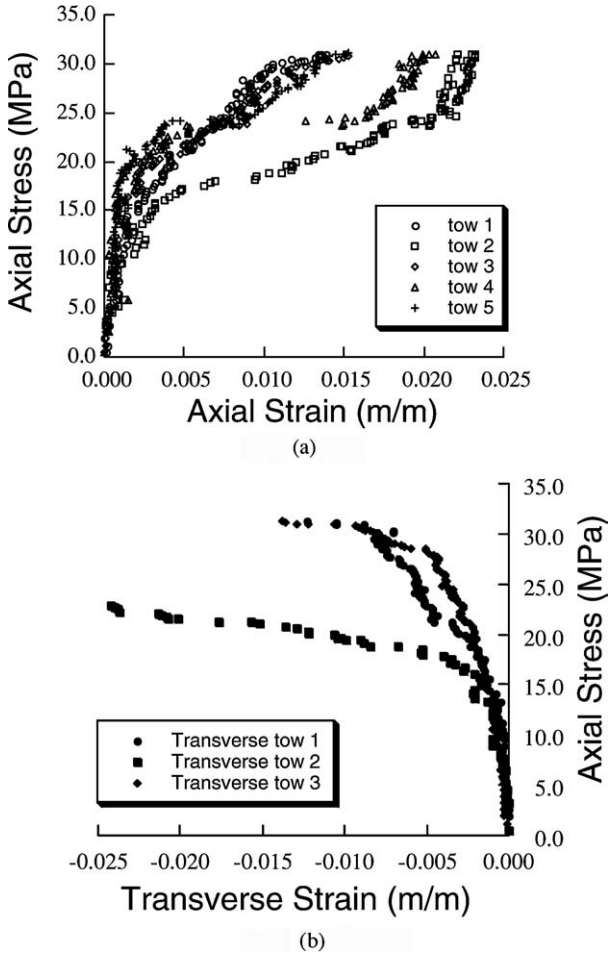

Figure 7 Axial and transverse strain response of each individual tow in a tensile specimen from the hybrid screen grid: (a) axial tows and (b) transverse tows.

of the $C_{(f)}/C$ panels was not consistent with that of typical monolithic engineering materials or woven composites due to the open cell network. Thus, an additional analysis was conducted to explore the effective uniaxial response in terms of the response of each tow.

According to the uniaxial behavior of the grids presented in Fig. 6, a two-stage response can be used to describe the fundamental mechanical response of the grids. Within the first stage of loading the curved axial tows were pulled in tension. Based on the sinusoidal shape that resulted from braiding (Fig. 2b) the axial tows were subjected to a combination of bending and tension with axial loading. Due to the shear stress imposed by bending and the relatively low interlaminar shear strength of the matrix the axial tows split along the neutral axis. Since the tow thickness (0.76 mm) of the accelerator grid was greater than that of the screen (0.51 mm), the curvature in the accelerator grid was larger and caused larger bending and interlaminar shear stresses. As a consequence, the oscillation in stiffness of the accelerator grids is far more pronounced than that in the screen grids as evident in Fig. 6. Splitting of the axial fibers resulted in a reduction of the curvature (straightening). The second stage of loading occurred as the delamination process reached saturation and was reflected by an increase in stiffness. Note that an increase in the effective stiffness is clearly evident for both the balanced and hybrid accelerator grids in Fig. 6c and d, respectively. The differences in axial fiber counts between the balanced and hybrid configurations also promoted differences in the constitutive behavior as reflected by the higher elastic modulus of the hybrid grid in comparison to the balanced accelerator grid. In contrast to the accelerator grids, the screen grids did not exhibit an increase in stiffness within the second stage of loading due to the lower fiber count and corresponding lower tensile strength.

The stress/strain response from the single tows in Fig. 9 was not fully consistent with the response for the grid in Fig. 6. Both the magnitude and frequency of oscillations in stiffness are less prevalent in the single fibers then evident in each individual tow of the multiple tow grids (Fig. 8). The differences suggest that the oscillation in stiffness was not only the consequence of interlaminar shear failure and straightening of the axial tows. It is reasonable to conclude that part of the oscillation in stiffness is also caused by the influence of the transverse tows, which are braided firmly with the axial tows. The transverse strain response for the balanced screen grid in Fig. 7b shows that one of the transverse tows had larger negative strain compared with the others. This particular transverse tow had debonded at some intersections with the axial tows and the response was therefore dominated by bending deformation due to normal forces imposed by straightening of the axial tows. In addition, there are two axial tows evident in Fig. 7a that underwent a larger deformation than the other tows. The larger axial deformation of these tows with loading can be attributed to debonding of these fibers from the transverse tows and/or unequal load distribution amongst the five tows of the specimen. It is useful to envision each axial tow as a series of springs subjected to an external load. If one of the springs in series undergoes a decrease in stiffness (due to interlaminar shear failure), the elongation in the remaining springs decreases even while the load is increasing. While this occurs, the load is transferred to the adjacent tows, which can also be considered as a system of springs in parallel. As a result, oscillation in the stress/strain response for each axial tow in the grid is more pronounced than that for the single tow presented in Fig. 8 due to the transfer of load from adjacent tows. For example, Fig. 8 shows the stress/strain response of each individual tow of the balanced accelerator grids (from Fig. 6a). Again, the tows were labeled "Tow #1" to "Tow #5" from the left. Tow #1 and Tow #5 were restrained by the transverse tows in only one direction and the oscillation in stiffness was less obvious than for those restrained at both sides. Thus, the unique constitutive response of the grids is also attributed to the influence of transverse fibers including displacement restraint and debonding. It is reasonable to assume that when the braided composites were subjected to tension the transverse tows partially restricted the axial tows from bending. The normal and shear stresses at all braided intersections caused bending of the transverse tows as well as sliding at the interface. This combined effect might lead to either debonding at the intersection or splitting of the

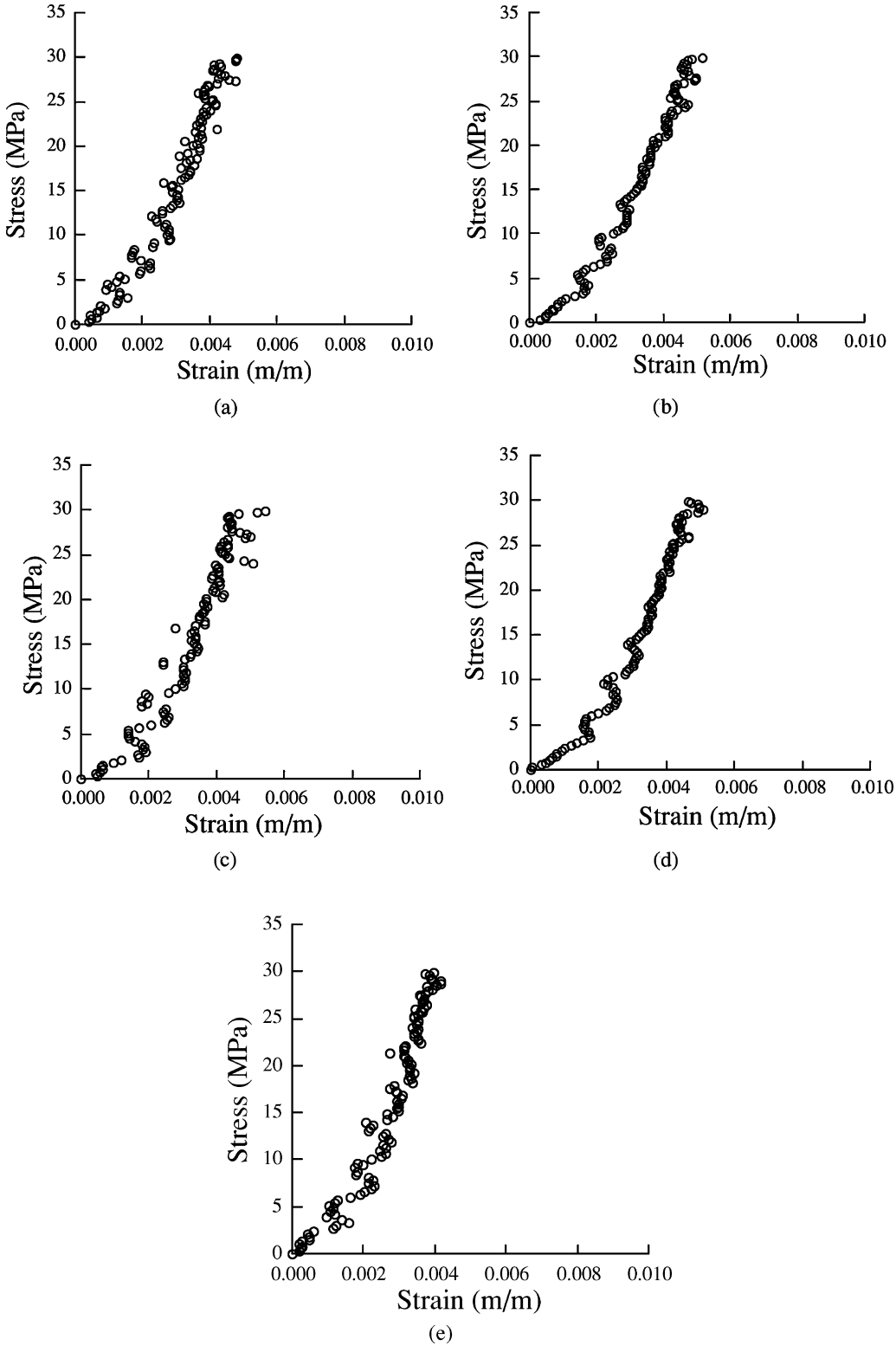

Figure 8 Axial response of the individual tows for the accelerator grid shown in Fig. 6c. The tows are identified from left to right: (a) tow 1, (b) tow 2, (c) tow 3, (d) tow 4 and (e) tow 5.

transverse tow along the axial direction, whichever is the weakest. Every time this happened a restraint was released which fostered a redistribution in stress within the axial tows. The events were evident through oscillation in the stress/strain response. Obviously, when the tensile load increased, the phenomenon happened more frequently as apparent by the increase in frequency of stiffness oscillations for the accelerator grid in Fig. 6. These aspects of mechanical behavior are important factors that will contribute to the next generation of grid designs. Without use of the optical biaxial extensometer it would have been almost impossible to understand the complicated uniaxial behavior of these systems.

The $C_{(f)}/C$ grids exhibited lighter weight and higher moduli than their molybdenum counterparts and in conjunction with predicted lower sputter erosion rates, appear to offer a viable alternative for "next generation"

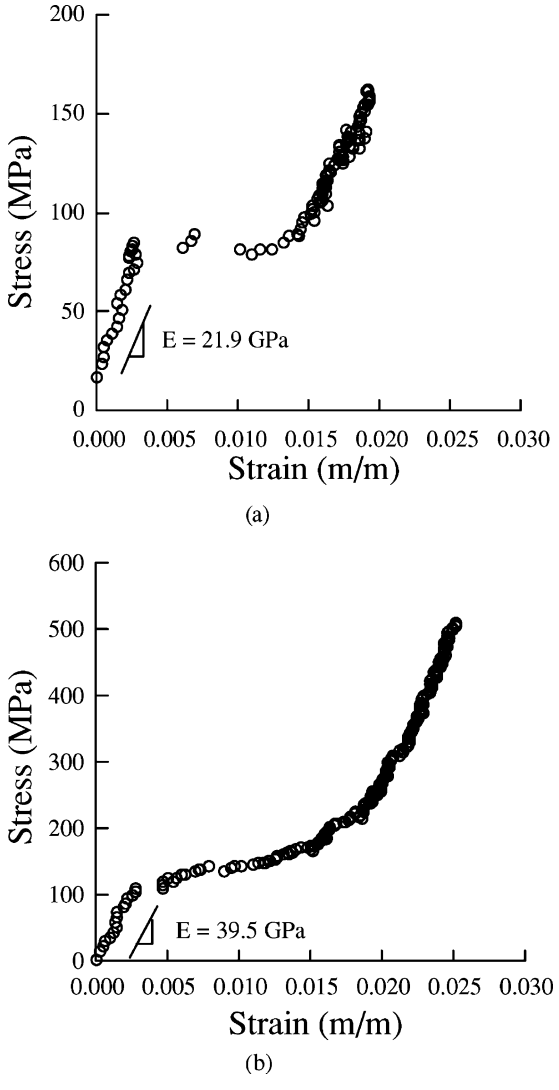

Figure 9 Uniaxial response of the carbon fiber tows tested in a single fiber arrangement: (a) screen tow (9 k fibers) and (b) accelerator tow (24 k fibers).

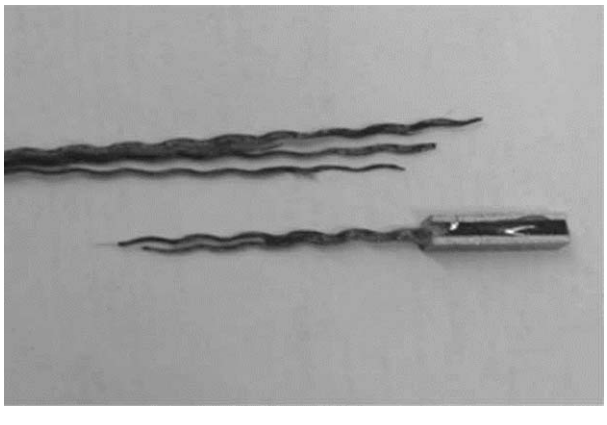

Figure 10 Delamination evident along the length of a single accelerator tow after failure.

ion propulsion engines [22]. Present efforts are aimed towards specific grid designs and improving the manufacturing techniques to improve the overall grid definition and woven surface topography. In the future, the stiffer $C_{(f)}/C$ grids may allow the fabrication of larger ion engines for higher power operation and mission lives in excess of 100,000 h.

6. Conclusion

Ceramic composite grid panels are presently being considered for use as the accelerator and screen grids in ion propulsion rocket engines. Four candidate carbon fiber composite ($C_{(f)}/C$) grids proposed for use in NASA's Evolutionary Xenon Thruster were fabricated. The constitutive behavior of the grids was examined under uniaxial tension and the displacement/strain distribution in the individual tows was determined using a specially designed optical extensometer based on digital image correlation (DIC). According to results from this experimental study the following conclusions were drawn:

(1) The effective elastic modulus for both the balanced and hybrid screen grids with axial fiber counts of 9 k and 18 k fibers was approximately 8.50 GPa. The elastic modulus for the balanced and hybrid accelerator grids ranged from 4.07 to 18.41 GPa.

(2) The stiffness of the screen grids decreased with axial load while the stiffness of the accelerator grids increased with axial load. The difference in mechanical behavior was due to the difference in tow cross-section of the screen and accelerator grids. The accelerator grids had a larger tow cross-section, which resulted in larger eccentric loads due to the tow curvature. The accelerator grids underwent larger elongation at low loads due to straightening of the fibers until a sufficient reduction in curvature promoted an increase in the fiber axial load.

(3) The biaxial optical extensometer based on DIC provided significantly more quantitative data that was useful in describing deformation of the axial and transverse tows. The system enabled a fundamental understanding of the mechanical behavior, which could not have been obtained with traditional measures of gage section elongation.

Acknowledgements

The authors would like to thank the technical point of contact, Fred Arnold at Wright Patterson Air Force Materials Laboratory for supporting this work under an IMWG funded PRDA Contract #F33615-01-C-5020 entitled "Low Cost C-C Ion Grids for High Power Ion Propulsion Engines". The authors would also like to thank Prabhakar Rao, Robert Reprogel, Wei Zheng and Dongliang Yang of the University of Maryland Baltimore County for technical support.

References

1. J. S. SOVEY, J. A. HAMLEY, T. W. HAAG, M. J. PATTERSON, E. J. PENCIL, T. T. PETERSON, L. R. PINERO, J. L. POWER, V. K. RAWLIN and C. J. SARMIENTO, AIAA Paper 97-2778, July 1997.
2. V. K. RAWLIN, J. S. SOVEY, J. A. HAMLEY, T. A. BOND, M. MATRANGA and J. F. STOCKY, AIAA Paper 99-4612, Sept. 1999.
3. J. E. POLK, J. R. ANDERSON, J. R. BROPHY, V. K. RAWLIN, M. J. PATTERSON, J. SOVEY and J. HAMLEY, AIAA Paper 99-2446, June 1999.
4. G. C. SOULAS, IEEE Aerospace Conference Paper 8.0303, March 2000.

5. *Idem.*, IEPC Conference Paper 01-090, Oct. 2001.
6. J. MUELLER, J. R. BROPHY and D. K. BROWN, AIAA Paper 96-3204, 1996.
7. T. W. HAAG and G. SOULAS, AIAA Paper 2002-4335, 2002.
8. W. N. SHARPE JR., *Exp. Mech.* **8** (1968) 164.
9. M. KUJAWINSKA and L. SALBUT, in Proceedings of SPIE—The International Society for Optical Engineering (2000) Vol. 4101, p. 380.
10. S. J. KIRKPATRICK and D. D. DUNCAN, in Proceedings of SPIE—The International Society for Optical Engineering (2000) Vol. 3914, p. 630.
11. L. SALBUT, in Proceedings of SPIE—The International Society for Optical Engineering (2002) vol. 4900, p. 1254.
12. T. LIU, F. AI-KHODAIRI, M. WU, M. IRLE and G. F. FERNANDO, in Proceedings of SPIE—The International Society for Optical Engineering (1996) Vol. 2895, p. 279.
13. C. T. PYE and J. MARTIN, *Sensors* **11** (1993) 10.
14. *Idem.*, *Materials World* **10** (1993) 557.
15. S. DAICOS and D. WIESE, *Exp. Tech.* **2** (1995) 13.
16. D. COIMBRA, R. GREENWOOD and K. KENDALL, *J. Mater. Sci.* **35** (2000) 3341.
17. W. H. PETERS and W. F. RANSON, *Opt. Eng.* **21** (1982) 427.
18. T. C. CHU, W. F. RANSON, M. A. SUTTON and W. H. PETERS, *Exp. Mech.* **25** (1985) 232.
19. H. A. BRUCK, S. R. MCNEILL, M. A. SUTTON and W. H. PETERS, *ibid.* **29** (1989) 261.
20. D. ZHANG and D. AROLA, in Proceedings of the SEM Annual Conference on Theoretical, Experimental and Computational Mechanics, Milwaukee, WI, June 2001, Paper No. 80.
21. L. A. CARLSSON and R. B. PIPES, "Experimental Characterization of Advanced Composite Materials (Prentice-Hall, Englewood Cliffs, NJ, 1987).
22. M. C. L. PATTERSON, P. WILBUR, W. ZIMBECK, F. ARNOLD, P. G. CHARALAMBIDES, D. AROLA and N. MECKEL, in Proceedings of the JANNAF Propulsion Meeting (Orlando, FL, Nov. 2002) p. 1.

Received 5 August 2003
and accepted 14 April 2004